Hyperuniformity on spherical surfaces

Ariel G. Meyra,[1,2] Guillermo J. Zarragoicoechea,[1,3] Alberto. L. Maltz,[4] Enrique Lomba ◉,[2] and Salvatore Torquato[5,6]

[1]*IFLYSIB (UNLP, CONICET), 59 No. 789, B1900BTE La Plata, Argentina*
[2]*Instituto de Química Física Rocasolano, CSIC, Calle Serrano 119, E-28006 Madrid, Spain*
[3]*Comisión de Investigaciones Científicas de la Provincia de Buenos Aires, Argentina*
[4]*Departamento de Matemática, Facultad de Ciencias Exactas, Universidad Nacional de La Plata,*
CC 72 Correo Central 1900 La Plata, Argentina
[5]*Department of Chemistry, Princeton University, Princeton, New Jersey 08544, USA*
[6]*Princeton Institute for the Science and Technology of Materials, Princeton University, Princeton, New Jersey 08544, USA*

We study and characterize local density fluctuations of ordered and disordered hyperuniform point distributions on spherical surfaces. In spite of the extensive literature on disordered hyperuniform systems in Euclidean geometries, to date few works have dealt with the problem of hyperuniformity in curved spaces. Indeed, some systems that display disordered hyperuniformity, like the spatial distribution of photoreceptors in avian retina, actually occur on curved surfaces. Here we will focus on the local particle number variance and its dependence on the size of the sampling window (which we take to be a spherical cap) for regular and uniform point distributions, as well as for equilibrium configurations of fluid particles interacting through Lennard-Jones, dipole-dipole, and charge-charge potentials. We show that the scaling of the local number variance as a function of the window size enables one to characterize hyperuniform and nonhyperuniform point patterns also on spherical surfaces.

I. INTRODUCTION

Since the fundamental work of Torquato and Stillinger in the early 2000s [1], hyperuniformity has been the focus of a large collection of works of relevance in the fields of physics (e.g. jammed packings [2,3], driven nonequilibrium granular and colloidal systems [4–6], sedimenting particle suspensions [7], sand piles and other avalanche models [8,9], and dynamical processes in ultracold atoms [10]), in materials science (photonic band-gap materials [11–13], dense disordered transparent dispersions [14], composites with desirable transport, dielectric and fracture properties [15–18], polymer-grafted nanoparticle systems [19], and "perfect" glasses [20]), and in biological systems (photoreceptor mosaics in avian retina [21] and immune system receptors [22]). The defining characteristic of these hyperuniform systems is the anomalous suppression of density (particle number or volume) variances at long wavelengths. In Euclidean space this implies that the structure factor $S(\mathbf{Q}) \equiv 1 + \rho \tilde{h}(\mathbf{Q})$ tends to zero as the wave number $Q \equiv |\mathbf{Q}| \to 0$ [1]:

$$\lim_{Q \to 0} S(\mathbf{Q}) = 0. \tag{1}$$

Here $\tilde{h}(\mathbf{Q})$ is the Fourier transform of the total correlation function $h(\mathbf{r}) = g_2(\mathbf{r}) - 1$, $g_2(\mathbf{r})$ is the pair correlation function, and ρ is the number density.

Hyperuniformity in most of the systems described above is a large-scale structural property defined in a Euclidean space [23]. However, generally speaking, one can also transfer the concept to consider point configurations in non-Euclidean spaces, such as points on the sphere or torus. A particular case of relevance in this connection is the avian photoreceptor

cells that are distributed on the retina [21], which is a curved surface. Obviously, to a first approximation, if the average near-neighbor distance between the receptors is small compared to the intrinsic curvature of the retina, one can reduce the problem to that of a particle distribution on a flat surface. However, this may not necessarily be the case in all instances, and hence curvature effects must be considered. The extension of the concept of hyperuniformity to sequences of finite point sets on the sphere was introduced in the very recent works of Brauchart and coworkers [24,25], where the problem is addressed from a formal mathematical perspective and connected to the more general problem of spherical designs. Point pattern designs on spherical surfaces are key in the development of optimal quasi-Monte Carlo (QMC) integration schemes [26]. These have been extensively used to construct efficient quadratures to evaluate illumination integrals, which are essential in the rendering of photorealistic images [27]. Brauchart and coworkers [24] have shown that these optimal QMC design sequences are hyperuniform. In Ref. [26] it was shown that good candidates to build QMC spherical designs could be devised from sets of points minimizing Coulomb or logarithmic (i.e., two-dimensional Coulomb) pairwise interactions. We will see here how this finding is reflected by our own results. Very recently, Božič and Čopar [28] have addressed the problem of hyperuniformity on the sphere and its connection with the spherical structure factor.

On the other hand, from a materials science perspective, the realization of particle designs on curved surfaces at the microscopic level has been experimentally achieved by means of self-assembly of colloidal particles on oil-glycerol interfaces [29]. This opens an avenue to experimentally devise and manipulate hyperuniform systems on curved surfaces at

will. Bearing in mind the relevance of hyperuniformity for the accurate representation of images (both in bird retina [21] and in artificial image rendering [27]), the potential impact of these experimental achievements on the design of artificial photoreceptor devices mimicking the acute visual system of birds is beneficial.

In order to further our understanding of hyperuniform systems in curved spaces, in this paper we have addressed the characterization of the local particle number variances on a collection of point and particle distributions on spherical surfaces. Our analysis encompasses both the canonical ensemble setting (fixed number of points) and the grand canonical ensemble (fluctuating number of points around some average value). On the other hand, one can resort to the use of the spherical structure factor as introduced by Brauchart *et al.* [24] and Franzini *et al.* [30]. In a recently published work, Božič and Čopar [28] suggest the presence of gaps at low multipole moments in this quantity as a signature of hyperuniformity. In this work, and in order to stress the direct connection with the characteristics of hyperuniformity in Euclidean space, we will focus on the density and number variances. Obviously, in the limit of infinite sphere radius with number density fixed, the properties of the system will approximate those of the Euclidean case, and Eq. (1) will be again useful as a signature of hyperuniformity. This large connection between curved and Euclidean geometries was already exploited by Caillol *et al.* [31] to remove the effects of periodic boundary conditions in molecular simulations and cope with the long range of Coulombic interactions without resorting to the use of Ewald summations or similar techniques.

In practice, here we will analyze the scaling of the local particle number variance defined as

$$\sigma_n^2(a) = \langle n(a)^2 \rangle - \langle n(a) \rangle^2, \tag{2}$$

where a denotes the base radius of the sampling spherical cap. This quantity is directly related to the sampling surface, s, as illustrated in Fig. 1. Also, in (2) $n(a)$ is the number of particles contained in the sampling window. The $\langle \cdot \rangle$ in Eq. (2) denotes an ensemble average on the spherical surface, as described in greater detail below. In practice, in this work we will be dealing with point distributions composed of finite sets of N points placed on the surface of a sphere of radius R and total area $A = 4\pi R^2$. From the work of Brauchart *et al.* [24], we
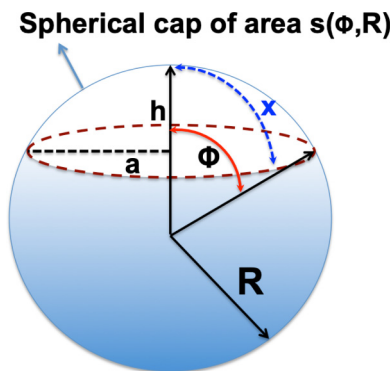
know that for uncorrelated points the local number variance scales with the surface of the sampling window, $\sigma_n^2(a) \sim s(a)$. In contrast, in hyperuniform systems, when $\rho^{-1/2} \ll a < R$, $\sigma_n^2(a)/s \to 0$.

In Sec. II we will introduce explicit expressions connecting the number variance with structural properties, such as the pair correlation function. In order to properly describe hyperuniformity on the curved sphere, in Sec. III we first analyze the behavior of the number variance of regular point patterns on the spherical surface, namely, a triangular grid and a Fibonacci lattice. Since translationally and orientationally ordered point patterns such as those of crystals in Euclidean space (or orientationally ordered, such as quasicrystals) are known to be hyperuniform, one should clearly expect the same to happen on the spherical surface. As reference nonhyperuniform point patterns, we investigate in Sec. IV uncorrelated point processes in both the canonical ensemble (uniform point distributions) and grand canonical ensembles (Poisson point distributions). In Sec. V we study the behavior of fluid particles confined on the spherical surface and interacting via potentials with different ranges, from short-range Lennard-Jones interactions to dipolar-like (i.e., $\sim r^{-3}$) and three-dimensional Coulomb (plasma-like) (i.e., $\sim 1/r$) interactions. To that aim we have performed canonical Monte Carlo simulations for various sphere sizes and a fixed surface density. We will see the correspondence between the hyperuniform and the nonhyperuniform reference systems on the spherical surface and in Euclidean space, and then we will see how the interactions and the size of the sphere play a role in the build up of disordered hyperuniform states on this non-Euclidean space. We make concluding remarks and discuss future prospects in Sec. VI.

II. EXPLICIT FORMULAS FOR THE NUMBER VARIANCE ON A SPHERE

To begin, consider a *single* configuration of a fixed number of points, N, on the 2-sphere $\mathbb{S}^2$, i.e., surface of a three-dimensional sphere of radius R, as depicted in Fig. 1. It is assumed that both N and R^2 are large and of comparable magnitude to one another. Let $a = \sqrt{h(2R - h)} \leqslant R$ and h denote the base radius and the height of a spherical cap, respectively. The surface area of a spherical cap is $s(a) = 2\pi R h = 2\pi R^2 [1 - \sqrt{1 - (a/R)^2}]$, where we will be considering only the upper hemisphere, $0 \leqslant \phi \leqslant \pi/2$, to avoid ambiguity. The number density of the points on the sphere is given by $\rho \equiv N/(4\pi R^2)$, and $n(\mathbf{x}_0; a)$ is the number of points contained within a spherical-cap window centered at position $\mathbf{x}_0$ on the sphere. Let the window uniformly sample the space for sufficiently small a, i.e., $s(a)$ is much smaller than $2\pi R^2$. Following Torquato and Stillinger [1] for the formulation in Euclidean space, the number variance associated with a single configuration on the sphere is given by

Spherical cap of area s(Φ,R)

FIG. 1. Spherical cap sampling region (white) of arc length x, area s, and base radius a, where the number variance is calculated.

$$\overline{n(a)^2} - \overline{n(a)}^2 = \rho s(a) \left[1 - \rho s(a) + \frac{1}{N} \sum_{\substack{i \neq j}}^{N} \alpha_2(x_{ij}; a) \right], \tag{3}$$

where $\overline{X}$ denotes a statistical average of a random variable X over uniformly distributed sampling windows on $4\pi R^2 \mathbb{S}^2$ and $\alpha_2(x; a)$ is the intersection area of two spherical caps whose centers are separated by a geodesic distance x, divided by the area of a cap. In analogy with the situation in Euclidean spaces [1], one can use formula (3) to find the particular point pattern that minimizes the variance at a fixed value of a, i.e., the ground state for the "potential energy" function represented by the pairwise sum in Eq. (3).

Now imagine that we generate many realizations of a large particle number N on the surface of the sphere so that the density is fixed and then consider the thermodynamic limit. The canonical ensemble-averaged number variance, $\sigma_n^2(a)$, follows immediately from Eqs. (2) and (3) by converting a summation to an integral involving $g_2(r)$:

$$\sigma_n^2(a) = \rho s(a)\left[1 - \rho s(a) + \rho\left(1 - \frac{1}{N}\right) \right.$$
$$\left. \times \int_{4\pi R^2 \mathbb{S}^2} g_2(x)\alpha_2(x; a)\, d\mathbf{x} \right], \quad (4)$$

where $g_2(x)$ is the geodesic pair correlation correlation function. Similarly, the corresponding ensemble-averaged expression for the local number variance in the grand canonical ensemble is also easily obtained from (2) and (3). We find

$$\sigma_n^2(a) = \langle\rho\rangle s(a)\left[1 - \langle\rho\rangle s(a) + \langle\rho\rangle \int_{4\pi R^2 \mathbb{S}^2} g_2(x)\alpha_2(x; a)\, d\mathbf{x} \right].$$
$$(5)$$

In the grand canonical ensemble, the number density of points fluctuates about some average value $\langle\rho\rangle$. Notice that formula (5) for the grand canonical ensemble is the one that most closely matches the local number variance formula in Euclidean spaces [1]. The reason for this is that in Euclidean space, hyperuniformity requires sampling large windows in infinite point sets; see Ref. [23] for further discussion on this point. It is noteworthy that when approaching the thermodynamic limit, results from Eqs. (4) and (5) are approximately the same for windows much smaller than the entire sphere surface ($\rho^{-1/2} \ll a \ll R$).

Brauchart *et al.* [26] rigorously studied the behavior of the number variance in the canonical ensemble in the large-N limit. For "uncorrelated" point patterns [i.e., $g_2(x) = 1$ for any x] in the canonical ensemble, from Eq. (4) one has

$$\sigma_n^2(a) = \rho s(a)\left[1 - \frac{s(a)}{4\pi R^2} \right], \quad (6)$$

where we have used the identity $\int_{4\pi R^2 \mathbb{S}^2} \alpha_2(x; a)\, d\mathbf{x} = s(a)$ and $N = 4\pi R^2 \rho$. Similarly, from Eq. (5) in the grand canonical ensemble, the number variance of "uncorrelated" point patterns satisfies

$$\sigma_n^2(a) = \langle\rho\rangle s(a), \quad (7)$$

because the second term and the integral in the square brackets of Eq. (5) exactly cancel each other. We call a point

process[1] on $\mathbb{S}^2$ in the canonical ensemble *hyperuniform* if as a increases in the scaling regime $1/\sqrt{\rho} \ll a < R$ $(1/\sqrt{\langle\rho\rangle} \ll a < R$ in the grand canonical):

$$\frac{\sigma_n^2(a)}{s(a)} \to 0. \quad (8)$$

In our particular case, from Brauchart *et al.* [25], the normalized intersection area is given by

$$\alpha_2(\psi; \phi) = 1 - \frac{1}{\pi \sin^2 \phi/2}\left[\arcsin\left(\frac{\sin \psi/2}{\sin \phi}\right) \right.$$
$$\left. - \arcsin\left(\frac{\tan \psi/2}{\tan \phi}\right)\cos \phi \right] \text{ if } \psi \leqslant 2\phi \quad (9)$$

and zero otherwise, where $\psi = x/R$ is the angle between the vectors pointing to the center of the two intersecting spherical caps. It can be shown that in the limit of $R \to \infty$, Eqs. (4) and (9) reduce to the expressions found in Ref. [1] for the Euclidean case in two dimensions.

III. NUMBER VARIANCE OF REGULAR POINT PATTERNS ON A SPHERICAL SURFACE

In this and the ensuing sections, we perform our analysis of the local particle number variance defined in Eq. (2) using a spherical cap as illustrated in Fig. 1.

First, we focus on the determination of the number variance associated with highly regular point patterns on the sphere, e.g., triangular lattices and Fibonacci lattices. Dealing with a regular point pattern implies that the spatial configuration of the points will be kept fixed. For this reason, and in order to perform an adequate sampling of the number variance, a sufficiently large number of centers of the sampling spherical cap must be chosen randomly on the surface (in our case around 10 000). In contrast, in the next sections (uncorrelated point patterns and fluid particles on a spherical surface), we will be able to average over multiple point configurations corresponding to the same density, ρ or $\langle\rho\rangle$.

It is important to note that building a two-dimensional lattice on an spherical surface is a nontrivial problem, which is certainly very useful in the field of astronomical observation. Here we will resort to the icosahedron method proposed by Tegmark [32] as an alternative for pixelizing the celestial sphere. The resulting point distribution is illustrated in Fig. 2(a). Note that this is an approximate triangular grid since the algorithm maps the triangular faces of an icosahedron in which the sphere is inscribed onto the surface of the sphere, and then distorts the points to give all pixels approximately the same area.

Another alternative that yields equal area for all grid points are the Fibonacci grids. Swinbank and Purser have proposed an efficient algorithm to produce this very regular grid on a spherical surface [33]. The corresponding illustration of the Fibonacci pattern is shown in Fig. 2(b). These procedures are

---

[1]A point process in Euclidean or compact spaces is a collection of point configurations that are specified by certain probability measures (see Ref. [23]).
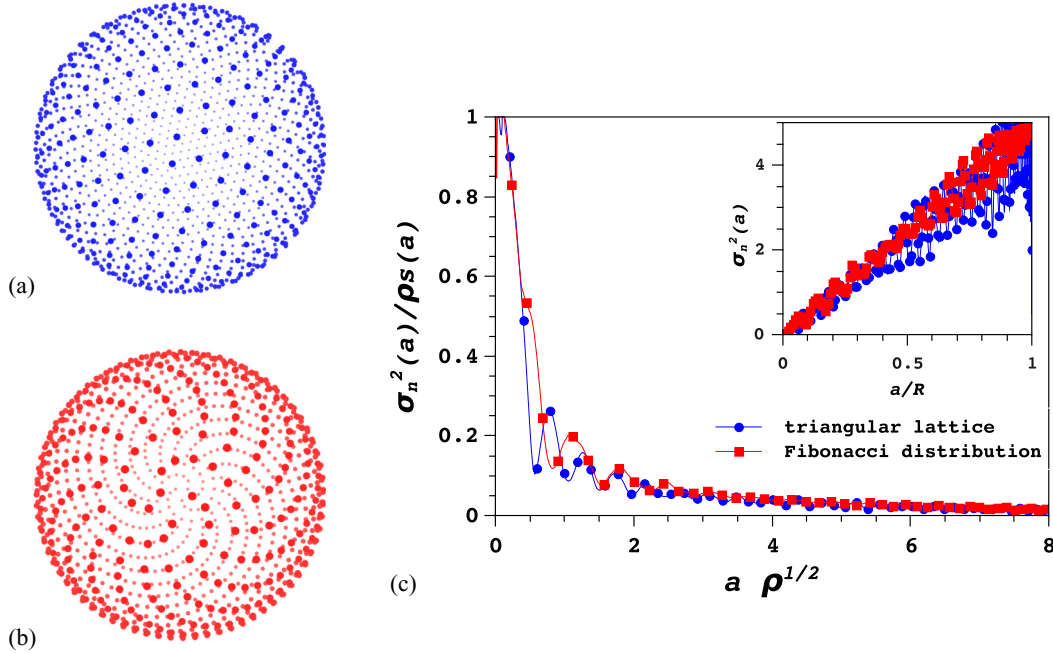
FIG. 2. Regular point distributions on a spherical surface: (a) Triangular lattice on a sphere, (b) Fibonacci distribution with 1000 points. (c) Plots of the scaled local number variance, $\sigma_n^2(a)/(\rho s)$, vs $a\rho^{1/2}$ as a signature of hyperuniformity [see Eq. (8)]. The inset illustrates the linear dependence of the number variance with the radius of the base of the sampling spherical cap (or the perimeter of the sampling window).

similar in spirit to the quasi-Monte Carlo approach for numerical integration on spherical surfaces discussed by Brauchart *et al.* [24]. In the latter instance, one must choose a set of points that minimizes the error of numerical integration, and this in turn leads to pixels of similar size on the sphere's surface. In Ref. [24] it was shown that this corresponds to a hyperuniform point distribution. The minimization constraint makes the approach deterministic, retaining nonetheless some Monte Carlo (i.e., stochastic) character. In contrast, the result of our two tessellation techniques would be the spherical geometry equivalent of regular grid integration sets in Euclidean spaces.

The $\sigma_n^2(a)/(\rho s)$ of the two regular point patterns is presented in Fig. 2(c). One observes clearly that these quantities decrease with a (in accordance with definition of Eq. (8) for hyperuniform systems). Obviously, a vanishing value is not to be reached due to the finite size of our systems. In the inset, in both instances one readily appreciates that the number variance scales linearly with the a, $\sigma_n^2(a) \propto a$, and hence also with the perimeter of the sampling area. This will precisely correspond to the linear dependence on the radius of the sampling window in perfectly ordered lattices in a flat two-dimensional space, as shown in Ref. [1]. In our study we have found that no simple scaling can be derived using the arc length, x, of the sampling spherical cap. The marked oscillations observed in σ_n^2 are a direct consequence of the ordering of the point patterns which is due to strong oscillations in $g_2(x)$ [cf. Eq. (4)], which is consistent with the previous observations in the behavior of the number variance of ordered point patterns in Euclidean spaces [1]. This quantity enters σ_n^2 through Eq. (4). We have thus identified the signatures of hyperuniformity on regular point patterns on the sphere.

IV. VARIANCES OF UNCORRELATED POINT DISTRIBUTIONS

In this section, we focus on the determination of the local number variances for uncorrelated point distributions, which serve as ideal reference nonhyperuniform systems. In the canonical ensemble, we consider uniform point patterns, N points uniformly distributed on the sphere. In the grand canonical ensemble, we consider Poisson point patterns, i.e., point configurations chosen from the Poisson distribution with the mean $\langle N \rangle$. Details on the algorithms to determine both types of point patterns can be found in the Appendix. Typical uniform and Poisson point patterns on the sphere are illustrated in Figs. 3(a) and 3(b), respectively.

Concerning the local number variance of point patterns following a random uniform distribution, we find that the analysis of $\sigma_n^2(a)$ for a wide range of particle numbers and sphere radius yields the simple relation $\sigma_n^2(a)/(\rho s) = 1 - s/(4\pi R^2)$, in agreement with Eq. (6). This can be expressed in terms of a/R to give $\sigma_n^2(a)/(\rho s) = \frac{1}{2}[1 + \sqrt{1 - (a/R)^2}]$ when $s(a) < 2\pi R^2$. Our results follow precisely this behavior, as clearly illustrated in the upper panel of Fig. 3(c). This result is in accordance with the known number variance of a uniform distribution on a plane for a finite system [24]. Note that clearly $\lim_{a\to\infty} \sigma_n^2(a)/(\rho s) \neq 0$, hence the system is not hyperuniform, as should be expected. From the above formulas it can be shown that $\sigma_n^2(a) \propto a^2$.

Let us now focus on the Poisson point distribution on a spherical surface, whose generation is not a straightforward process. Here point patterns are generated by an algorithm devised by Baddeley [34], which is described in the Appendix. A characteristic Poisson configuration on the spherical surface is illustrated in Fig. 3(b). Note that the configurations so
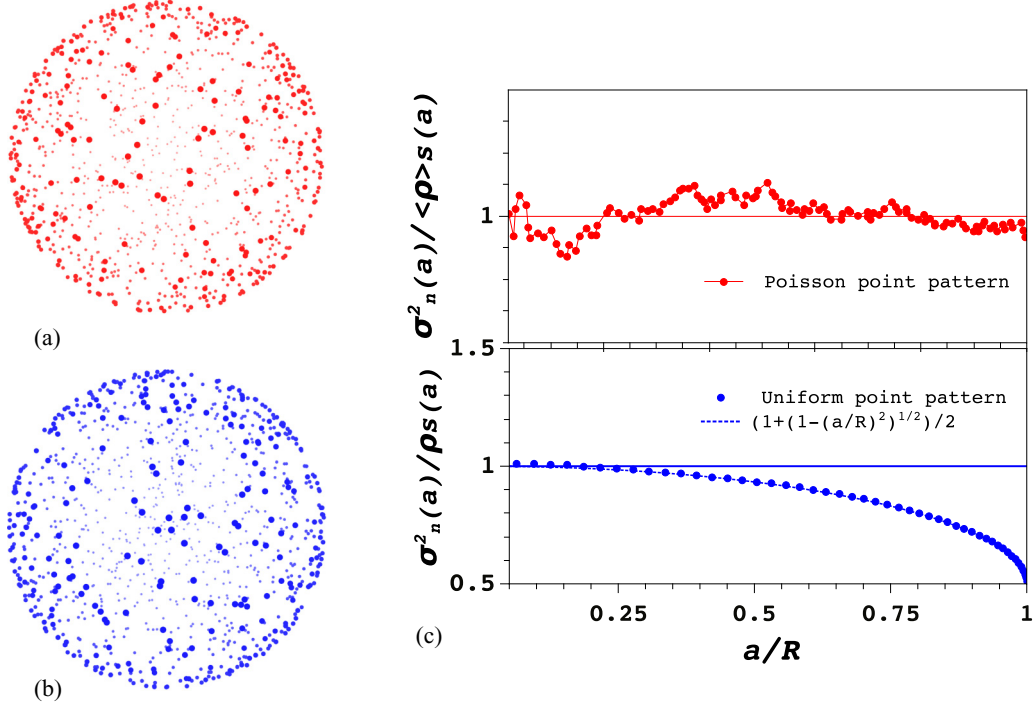
FIG. 3. Uncorrelated point patterns on a sphere in both the grand canonical (a) Poisson distribution (R = 1, $\langle N \rangle = 750$) and canonical (b) uniform distribution ensembles. (c) Plots of the scaled number variance $\sigma_n^2(a)/\rho s$ in terms of a for the uniform (lower) and Poisson point patterns (upper). In agreement with Eqs. (4) and (5), the number variance of the Poisson point pattern can be seen to follow approximately Eq. (7), whereas the variance for the uniform point pattern follows $\sigma_n^2(a)/(\rho s) = [1 + \sqrt{1 - (a/R)^2}]/2$ [Eq. (6)].

generated will be characterized by an average surface density, $\langle \rho \rangle$, and in contrast with the previously discussed uniform distribution, we will not have a system with a fixed number of points, N. Instead we will have a collection of systems that have the average density, $\langle \rho \rangle$. As mentioned before, to some extent, this formulation recalls the relation between grand canonical and canonical ensembles. We now observe that $\sigma_n^2(a)/(\langle \rho \rangle s) \sim 1$ as expected from an uncorrelated point process [cf. Eq. (7)], and it is a known result for the Poisson point distribution on a plane as well [34].

In summary, when considering systems with a fixed number of points, N, in analogy with the definitions for Euclidean spaces, a scaling $\sigma_n^2(a) \propto a^2$ will be associated with a nonhyperuniform point distribution. In the particular case of Poisson patterns $\sigma_n^2(a) \propto s$ will be the sought signature.

In this way, we have defined what will be our reference results for scaling of the local number variance on the spherical surface for configurations with a fixed number of points. We will see within the scaling regime $\rho^{-1/2} \ll a < R$, intermediate situations between linear and quadratic scaling will also be possible, such that

$$\sigma_n^2(a) \propto a^\delta \quad \text{with} \quad 1 < \delta < 2. \tag{10}$$

From Eq. (8), these values of δ will also correspond to hyperuniform configurations so that the scaled variance $\sigma_n^2(a)/(\rho s)$ decreases as a decreases. A summary of the systems considered up to this point is collected in Table I together with those of fluid configurations on the spherical surface.

V. NUMBER VARIANCES IN FLUIDS OF INTERACTING PARTICLES

In this section, we present some results of Monte Carlo simulations in a canonical ensemble (with a prescribed particle number N, system area A, and temperature T) for particles on a spherical surface interacting with the potential

TABLE I. Summary of the scaling behavior of the number variance with the geometric parameters of the sampling window for uncorrelated, regular point patterns, and fluid configurations on the sphere. In the latter instance, results for two different radii are presented.

Point pattern	Scaling
Poisson distribution	$\sigma_n^2(a) \propto s = (1 - \sqrt{1 - (a/R)^2}) 2\pi R^2$
Uniform distribution	$\sigma_n^2(a) \propto a^2 = s(1 - s/(4\pi R^2))/\pi$
Triangular lattice	$\sigma_n^2(a) \propto a$
Fibonacci lattice	$\sigma_n^2(a) \propto a$
$R = 15$	
LJ fluid	$\sigma_n^2(a) \propto a^2$
$U_{dd}(\alpha = 1)$	$\sigma_n^2(a) \propto a^2$
$U_{dd\parallel}(\alpha = 1)$ fluid	$\sigma_n^2(a) \propto a^{1.8}$
$U_{dc}(\gamma = 1)$ fluid	$\sigma_n^2(a) \propto a^{1.7}$
$U_{cc}(\beta = 1)$ fluid	$\sigma_n^2(a) \propto a^{1.4}$
$R = 5$	
$U_{dd\parallel}(\alpha = 1)$ fluid	$\sigma_n^2(a) \propto a^{1.7}$
$U_{dd\parallel}(\alpha = 3)$ fluid	$\sigma_n^2(a) \propto a^{1.3}$
$U_{dd\parallel}(\alpha = 6)$ fluid	$\sigma_n^2(a) \propto a^{1.1}$

functions summarized below in Eqs. (11) and (12a)–(12d). The simulation starts when N particles are randomly placed on a sphere surface of radius R. We then perform 5×10^5 translational attempts along random directions on the surface in order to equilibrate the system. Averages are calculated over 10^5 statistically independent configurations. Sampling of the number variance is performed using only three different coordinate origins in orthogonal directions. Here we will analyze the effect of different interactions on the local particle number variances. Bearing in mind the results of the previous section, we will be able to see how the interaction tunes the hyperuniform character of the fluid structure.

The net pair interaction between particles i and j has a short-range dispersive and repulsive component of the Lennard-Jones (LJ) form:

$$U_{LJ}(r) = 4\epsilon \left[\left(\frac{d_{LJ}}{r} \right)^{12} - \left(\frac{d_{LJ}}{r} \right)^{6} \right], \quad (11)$$

where r is the Euclidean distance between particles i and j, and not the arc length. The Lennard Jones parameters, ϵ and d_{LJ}, are defined as units of energy and length, respectively. We set the reduced temperature to $T^* = k_B T/\epsilon = 5.2$ (k_B being Boltzmann's constant), which is well above the critical temperature for a LJ fluid. To the LJ interaction we will add dipolar-like, charge-dipole, and charge-charge contributions. To simplify the problem, dipoles are kept perpendicular to the surface, as if under the influence of an electric field whose source is at the center of the sphere. We will also consider the case of a simple $1/r^3$ repulsion (equivalent to that of completely parallel dipoles on a plane), and for the charge-dipole interaction we will also consider that dipoles are orthogonal to the line joining the particle centers. This is a crude approximation to the case of dipoles perpendicular to the surface. The explicit form of the interactions used is

$$U_{dd}(r, \vec{s}_i, \vec{s}_j) = U_{LJ}(r) + \frac{\alpha}{r^3} \left[(\vec{s}_i \cdot \vec{s}_j) - \frac{3(\vec{s}_i \cdot \vec{r})(\vec{s}_j \cdot \vec{r})}{r^2} \right], \quad (12a)$$

$$U_{dd||}(r) = U_{LJ}(r) + \frac{\alpha}{r^3}, \quad (12b)$$

$$U_{dc}(r) = U_{LJ}(r) + \frac{\gamma}{r^2}, \quad (12c)$$

$$U_{cc}(r) = U_{LJ}(r) + \frac{\beta}{r}, \quad (12d)$$

where γ, $\beta = 1$ and α will be set to unity in most cases, except when analyzing the effect of the repulsion strength on the number variance and pattern formation, and $\vec{s}_i$ ($\vec{s}_j$) is the unit vector denoting the orientation of dipole i (j).

We have first determined the local number variance for particle configurations on a sphere of radius $R = 15$. Results are presented in Fig. 4. In the inset two reference curves have been added, one representing the linear dependence on the sampling window radius, a (hyperuniform scaling in ordered configurations) and another for the quadratic dependence (regular disordered nonhyperuniform systems). Note that here we have plotted a normalized variance $\sigma_n^{2*}(a)$, scaled with the value of $\sigma_n^2(a = R)$ (obtained for each realization). One immediately observes that as the range of the potential increases, the scaling becomes hyperuniform, i.e., $\sigma_n^2(a) \propto a^\delta$
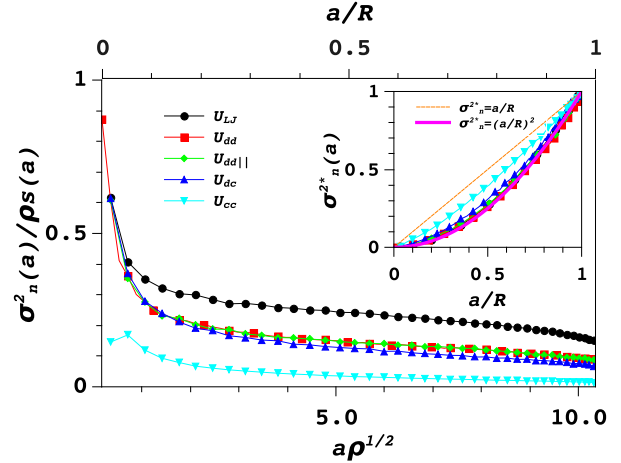

FIG. 4. Plots of the scaled particle number variance, $\sigma_n^2(a)/[\rho s(a)]$, vs $a\rho^{1/2}$, for configurations of particles interacting with various potentials (as shown in the legend), on a sphere of radius $R = 15$ and for a density $\rho = 0.5$. One can appreciate that curves are grouped following the range of the interaction, LJ (upper curve, nonhyperuniform), dipole-dipole and dipole charge, and charge-charge (both hyperuniform). In the inset the normalized number variance is plotted as a function of a to illustrate the deviation from the linear behavior (hyperuniform scaling for regular configurations) as the range of the interaction decreases, to finally reach almost quadratic scaling (nonhyperuniform) for the LJ interaction. We note that the precipitous drop of the scaled number variance $\sigma_n^2(a)/[\rho s(a)]$ for very small values of a will occur for any correlated system, whether hyperuniform or not, in both curved and flat spaces.

with $\delta < 2$, and δ decreasing as the interaction range increases. In fact, for the Coulomb-like interaction we have $\delta \approx 1.4$. This interaction gives strictly $\delta = 1$ for planar surfaces [35]. The pure LJ fluid, as in the Euclidean case, displays no hyperuniformity and conforms quadratic scaling as the uniform random point patterns. In the main graph of Fig. 4 we have plotted $\sigma_n^2/(\rho s)$, and we find again here that as the range of the interaction increases this quantity tends to vanish as a grows. The results for the LJ are qualitatively similar to those of the uniform random distribution depicted in Fig. 3(c), in accordance with the quadratic scaling illustrated in the inset. Values of the exponent δ obtained from fits of $\sigma_n^2(a) \propto a^\delta$ are collected in Table I, together with results obtained for $R = 5$ and the same density with varying interaction strength. Interestingly, one can observe that dipoles perpendicular to the spherical surface display a quadratic scaling identical to that of the LJ fluid, i.e., $\delta = 2$. This is due to the fact that the angular part of the interaction changes, including becoming attractive when the sign changes, as the dipoles move apart due to the curvature of the sphere. Due to this, the long-range component of the interaction is not purely repulsive anymore, a requirement that must be fulfilled in disordered systems that exhibit hyperuniformity for equilibrium states at finite temperature [36]. This situation is in marked contrast with that of dipoles orthogonal to a plane, where the interaction is always purely repulsive and long-ranged, i.e. exactly the interaction defined by Eq. (12b), $U_{dd||}(r)$. We see in Fig. 4 that for this long-range interaction the scaling begins to deviate
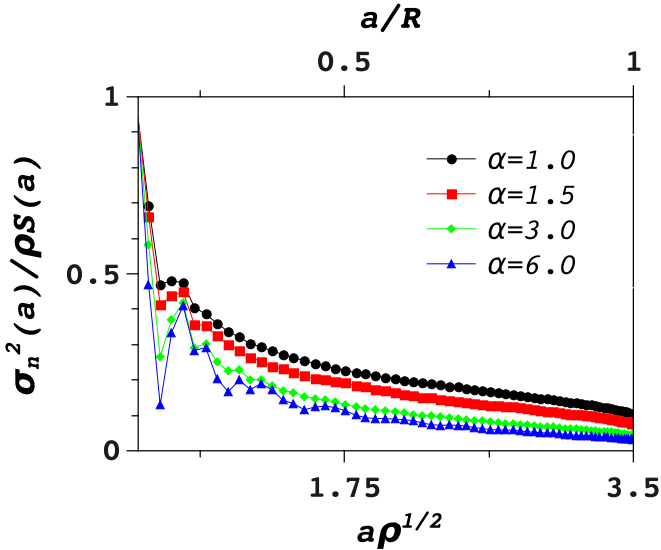
FIG. 5. Scaled number variance, $\sigma_n^2(a)/(\rho s)$, vs the radius of the sampling surface, $a\rho^{1/2}$, for a system of particles with parallel dipole-dipole interactions Eq. (12b) in terms of the α parameter. Particles lie on a sphere of radius $R = 5$, with a reduced density $\rho = 0.5$. The system becomes more hyperuniform as the strength of the interaction (α) increases.

from that of the LJ (quadratic), with an exponent $\delta = 1.8$ (see Table I).

It has to be pointed out that in Fig. 4 we have omitted the results for $a < 1$, a region where one should see that $\lim_{a\to 0} \sigma_n^2(a)/(\rho s) = 1$. When $a < 1$, the sampling window is smaller than the particle size, which implies that one cannot expect to obtain a statistically significant value for the variance along a finite simulation run, particularly as $a \to 0$. This limitation applies more drastically to the results presented in Fig. 5, since they correspond to a smaller sample size.

Now, instead of tuning the interaction range by changing the functional form of the long-range contribution to the potential as done above, we can modify its intensity (which is in part equivalent to lowering the temperature). Here we have chosen to vary the α parameter in $U_{dd\parallel}$ [Eq. (12b)] from 1 to 6 for $R = 5$ and $\rho = 0.5$. The effect of this change on the local number variance is visible in the plot of Fig. 5. One can clearly observe that as the strength of the interaction increases

the degree of hyperuniformity grows. This should not be surprising, since for a finite system increasing α is to some extent equivalent to an increase in the range of interaction. For $\alpha = 6$ we are back to the linear scaling (strong hyperuniformity), as evidenced by the value $\delta = 1.1$ in the scaling of Table I. One can also appreciate the characteristic oscillations of a regular pattern. This pattern formation is readily seen in the snapshots of Fig. 6. One sees there that for the largest interaction strength the particles are almost ordered in a triangular lattice. This is mostly an energetic effect (even if entropy is also maximized), by which the particles adopt a configuration that maximizes the interparticle distances, thus minimizing the repulsive energy. With this quasi-ordered state we are back to the purely linear dependence of the local number variance of the triangular and Fibonacci lattices. These low-temperature (or high-α) states recall the point patterns that minimize the Coulomb energy, which according to Ref. [26] provide suitable spherical designs for QMC integration.

Finally, another feature that must be commented upon is the visible decrease of the slope of the curves of the local number variance in Figs. 4 and 5 and also in Fig. 8 (becoming more negative as the interaction becomes weak) that can be appreciated as $a/R \to 1$. This is the result of performing the calculations for a finite-sized sample in the canonical ensemble, which is contributed from the following term in Eq. (4):

$$-\frac{\rho}{N}\int g_2(x)\alpha_2(x, a)\, d\mathbf{x}. \qquad (13)$$

This term becomes more negative and has a larger contribution to $\sigma_n^2(a)$ as $a/R \to 1$. This feature is also evident in the upper panel of Fig. 3(c). This case is particularly meaningful since now the term (13) reduces to $-s(a)/(4\pi R^2)$. This contribution is absent in the grand canonical case. Comparing the upper and lower panels of Fig. 3(c) (canonical vs grand canonical ensemble), one can immediately grasp the implications of using a given ensemble well away from the thermodynamic limit.

All other intermediate disordered situations are also hyperuniform, but interestingly none of them (and neither does the pure Coulomb repulsion) exhibits the scaling $\sigma_n^2(a) \sim a$ at positive temperatures. This is in contrast with the situation found for plasmas in Euclidean space [35,36] which produce structural hyperuniform configurations with linear scaling at any finite temperature.
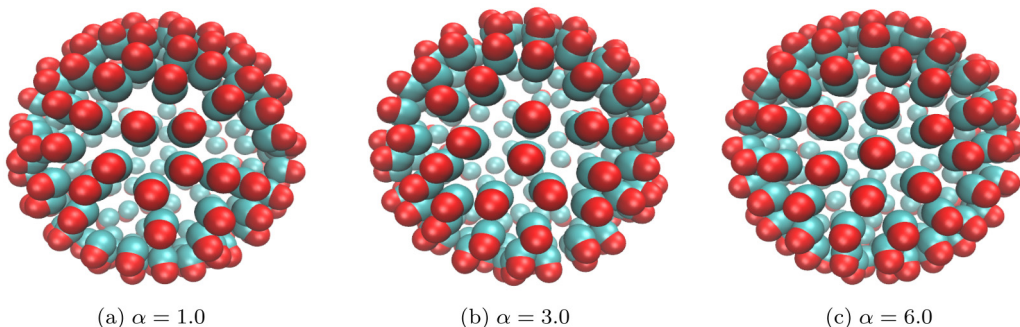

FIG. 6. Illustration of simulated systems for representative states of different repulsion strength when the long-range interaction is $U_{dd\parallel}$ [cf. Eq. (12b)]. For illustrative purposes, samples presented here are smaller than the samples that we use to compute the local number variances.
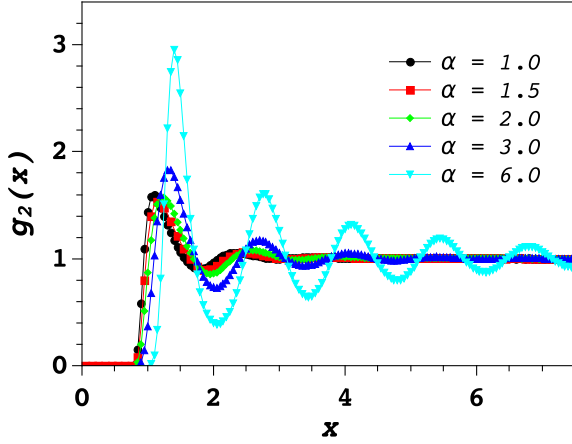
FIG. 7. Effect of the interaction strength on the pair correlation for a fluid with dipole-dipole-like interactions on a sphere of radius $R = 5$ and with surface density $\rho = 0.5$. Here x is the geodesic distance between two particles.

The structuring of the fluid as a consequence of the increasing interaction strength is clearly reflected by the pair correlation function depicted in Fig. 7. Here the build up of strong short-range order is seen in the marked oscillations of $g_2(r)$ for $\alpha = 6$. This short-range order is, however, highly distorted for distances beyond the second coordination shell due to thermal fluctuations. These changes on the pair correlation function induced by the increase on the interaction strength are also reflected on the evolution of the number variance with the size of the sampling window through Eq. (4) in Fig. 8. The results qualitatively agree with those of Fig. 5 computed by direct MC sampling of the particle number variance. One observes how the results for $\sigma_n^2(a)/\rho s$ computed from Eq. (4) fall below the uniform limit value ($=1$) and decrease as the repulsive strength increases, albeit with the results for $\alpha = 1$ slightly closer to those of the LJ fluid. This behavior is

in accordance with the qualitative behavior observed in the curves of Figs. 4 and 5. For small sampling window sizes, the agreement becomes quantitative. On the other hand as a grows, the integrated value of $\sigma_n^2(a)$ increasingly deviates from the MC results because this integral is appreciably affected by statistical uncertainties in the tail of $g_2(r)$.

VI. CONCLUSIONS

In summary, we presented derivations of formulas for the local number variance of point patterns on the sphere in both the canonical and grand canonical ensembles. We demonstrated that uncorrelated point patterns in these two ensembles are definitely not hyperuniform and their corresponding variance behaviors can dramatically differ for large windows. We also showed that the local number variance exhibits two distinct types of hyperuniform scalings in the canonical ensemble: regular point patterns have a scaling $\sigma_n^2(a) \sim a$, and some correlated disordered point patterns have $\sigma_n^2(a) \sim a^\delta (1 < \delta < 2)$, which correspond to class I and class III in Euclidean spaces [23], respectively. There are also certain hyperuniform point patterns that correspond to class II in Euclidean space [23], e.g., determinantal point patterns in the so-called harmonic ensemble [25], although they were not classified that way in Ref. [25]. The identification and classification of hyperuniform point configurations on the sphere and other compact spaces (such as cylinders, ellipsoids, or tori) represent a largely open area for future research. We also plan to study the effect of interactions that favor the formation of quasicrystal-like structures, in particular those that present highly directional bonding interactions, as found in patchy colloids.

APPENDIX: GENERATING UNCORRELATED POINT PATTERNS

1. Uniform point patterns

The generation of a uniform point configuration is a trivial problem in Euclidean spaces using pseudorandom numbers. On a spherical surface $\mathbb{S}^2$, however, one must be a bit more careful. The simplest approach is to generate a uniform distribution of points inside a cube inscribing the sphere, discarding those points outside the sphere, and then performing an orthogonal projection of the inner points onto the surface [37]. Alternatively one can choose three pseudorandom numbers following a Gaussian distribution centered in the sphere of radius, R, and project the resulting points in space onto the
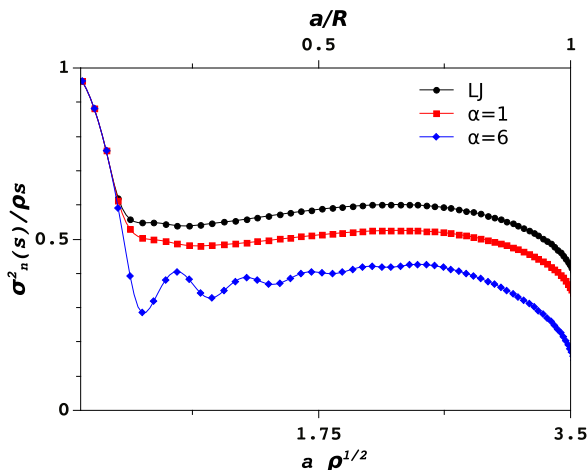

FIG. 8. Scaled number variance $\sigma_n^2(a)/\rho s$ vs $a\rho^{1/2}$ as calculated from the pair correlation functions from Eq. (4) for the LJ and dipolar-like interactions with increasing repulsive strength ($\rho = 0.5$, $R = 5$). The strong oscillations in $g_2(x)$ seen in Fig. 7 are reflected in the curve for $\alpha = 6$.

spherical surface. Other approaches can also be found in Ref. [38].

2. Poisson point patterns

We recall that a random variable whose values are the nonnegative integers has a Poisson distribution with parameter $\lambda > 0$ whenever $P[X = k] = e^{-\lambda}\lambda^k/k!$ for $k = 1, 2, \ldots$. It is often abbreviated by saying that X has a Poiss(λ) distribution. Note that λ corresponds specifically to $\langle \rho \rangle$ in the main text. Some basic properties are the following:

(1) If X follows a Poisson distribution with an intensity λ [i.e., $X \sim$ Poiss(λ)], then $E(X) = \text{Var}(X) = \lambda$.

(2) If $X_1, \ldots, X_n$ are independent random variables having Poiss(λ_1), $\ldots$, Poiss(λ_n) distributions, respectively, then $X_1 + \cdots + X_n$ has a Poiss($\lambda_1 + \cdots + \lambda_n$) distribution.

Let S be a sphere. For each region $A \subseteq S$ we denote its area by $\mu(A)$. Suppose that we have a random distribution of points on the sphere. For each region $A \subseteq S$ we denote $N(A)$ the random variable "number of points in A." We have a random spatial point process with parameter $c > 0$ whenever

(1) For each A, $N(A)$ has a Poiss[$c\mu(A)/\mu(S)$] distribution.

(2) If $A_1, \ldots, A_n$ are mutually disjoint regions, then $N(A_1), \ldots, N(A_n)$ are independent random variables.

We recall that each point in the sphere has two angular spherical coordinates θ and ϕ. In order to generate a set of points distributed according to a Poisson spatial process on the sphere with parameter c we have developed an algorithm based in an usual idea in this subject:

(1) We subdivide the sphere into small, mutually disjoint "spherical rectangles" $R_1, \ldots, R_m$ so that the angular coordinates (θ, ϕ) of every point in R_j satisfy inequalities of the form $\theta_{j1} < \theta \leqslant \theta_{j2}$ and $\phi_{j1} < \phi \leqslant \phi_{j2}$.

(2) For each R_j we generate a random number k_j according to a Poiss[$c\mu(R_j)/\mu(S)$] distribution and k_j points uniformly distributed in R_j are generated.

[1] S. Torquato and F. H. Stillinger, Phys. Rev. E **68**, 041113 (2003).

[2] A. Donev, F. H. Stillinger, and S. Torquato, Phys. Rev. Lett. **95**, 090604 (2005).

[3] D. Hexner, A. J. Liu, and S. R. Nagel, Phys. Rev. Lett. **121**, 115501 (2018).

[4] D. Hexner and D. Levine, Phys. Rev. Lett. **114**, 110602 (2015).

[5] J. H. Weijs, R. Jeanneret, R. Dreyfus, and D. Bartolo, Phys. Rev. Lett. **115**, 108301 (2015).

[6] E. Tjhung and L. Berthier, Phys. Rev. Lett. **114**, 148301 (2015).

[7] J. Wang, J. M. Schwarz, and J. D. Paulsen, Nat. Commun. **9**, 2836 (2018).

[8] R. Dickman and S. D. da Cunha, Phys. Rev. E **92**, 020104(R) (2015).

[9] R. Garcia-Millan, G. Pruessner, L. Pickering, and K. Christensen, Europhys. Lett. **122**, 50003 (2018).

[10] I. Lesanovsky and J. P. Garrahan, Phys. Rev. A **90**, 011603(R) (2014).

[11] M. Florescu, S. Torquato, and P. J. Steinhardt, Proc. Nat. Acad. Sci. USA **106**, 20658 (2009).

[12] W. Man, M. Florescu, E. P. Williamson, Y. He, S. R. Hashemizad, B. Y. C. Leung, D. R. Liner, S. Torquato, P. M. Chaikin, and P. J. Steinhardt, Proc. Nat. Acad. Sci. USA **110**, 15886 (2013).

[13] L. S. Froufe-Pérez, M. Engel, J. José Sáenz, and F. Scheffold, Proc. Nat. Acad. Sci. USA **114**, 9570 (2017).

[14] O. Leseur, R. Pierrat, and R. Carminati, Optica **3**, 763 (2016).

[15] G. Zhang, F. H. Stillinger, and S. Torquato, J. Chem. Phys. **145**, 244109 (2016).

[16] D. Chen and S. Torquato, Acta Mater. **142**, 152 (2018).

[17] Y. Xu, S. Chen, P.-E. Chen, W. Xu, and Y. Jiao, Phys. Rev. E **96**, 043301 (2017).

[18] B.-Y. Wu, X.-Q. Sheng, and Y. Hao, PloS ONE **12**, e0185921 (2017).

[19] A. Chremos and J. F. Douglas, Ann. Phys. (Berlin) **529**, 1600342 (2017).

[20] G. Zhang, F. H. Stillinger, and S. Torquato, Phys. Rev. E **96**, 042146 (2017).

[21] Y. Jiao, T. Lau, H. Hatzikirou, M. Meyer-Hermann, J. C. Corbo, and S. Torquato, Phys. Rev. E **89**, 022721 (2014).

[22] A. Mayer, V. Balasubramanian, T. Mora, and A. M. Walczak, Proc. Nat. Acad. Sci. USA **112**, 5950 (2015).

[23] S. Torquato, Phys. Rep. **745**, 1 (2018).

[24] J. S. Brauchart, P. J. Grabner, and W. B. Kusner, Constr. Approx. **50**, 45 (2019).

[25] J. S. Brauchart, P. J. Grabner, W. B. Kusner, and J. Ziefle, arXiv:1809.02645v1 (2018).

[26] J. S. Brauchart, E. B. Saff, I. H. Sloan, and R. S. Womersley, Math. Comput. **83**, 2821 (2014).

[27] R. Marques, C. Bouville, L. P. Santos, and K. Bouatouch, Synth. Lect. Comput. Graphics Animation **7**, 1 (2015).

[28] A. L. Božič and S. Čopar, Phys. Rev. E **99**, 032601 (2019).

[29] W. T. Irvine, M. J. Bowick, and P. M. Chaikin, Nat. Mater. **11**, 948 (2012).

[30] S. Franzini, L. Reatto, and D. Pini, Soft Matter **14**, 8724 (2018).

[31] J. M. Caillol, D. Levesque, and J. J. Weis, Mol. Phys. **44**, 733 (1981).

[32] M. Tegmark, Astrophys. J. **470**, L81 (1996).

[33] R. Swinbank and R. Purser, Q. J. R. Meteorol. Soc. **132**, 1769 (2006).

[34] A. Baddeley, in *Stochastic Geometry*, edited by W. Weil (Springer, Berlin, 2004), pp. 1–75.

[35] E. Lomba, J.-J. Weis, and S. Torquato, Phys. Rev. E **97**, 010102(R) (2018).

[36] E. Lomba, J. J. Weis, and S. Torquato, Phys. Rev. E **96**, 062126 (2017).

[37] J. M. Cook, Math. Tables Aids Comput. **11**, 81 (1957).

[38] E. Weisstein, Sphere point picking, MathWorld. http://mathworld.wolfram.com/SpherePointPicking.html (2018).